Interpolation Technique for Computational Aeroacoustics and Vibroacoustics

Stefan Schoder[1], Manfred Kaltenbacher[1]

[1] *TU Wien Institut für Mechanik und Mechatronik, 1060 Wien, Österreich, Email: stefan.schoder@tuwien.ac.at*

Introduction

Since the beginning of computational aeroacoustics (CAA), hybrid methodologies have been established as the most practical methods for aeroacoustic computations. In aeroacoustics, the well known disparity of length scale for low Mach number flows causes a very efficient computational procedure and well suited simulation models using different meshes for flow and acoustics. The workflow of these aeroacoustic approaches is based on three steps: (1) perform unsteady flow computations based on an appropriate turbulence model on a restricted sub-domain; (2) compute the acoustic sources; (3) simulate the acoustic field. It should be noted that analog to aeroacoustics, decoupled vibro-acoustic simulations follow a similar three step approach, aiming to compute the acoustic field due to structural deformations.

We analyze the second step of the hybrid aeroacoustic workflow. Desirably, an accurate, flexible, and conservative coupling scheme ensures a rigorous connection between fluid dynamics and acoustics within a hybrid aeroacoustic simulation. The properties of the coupling scheme, respectively interpolation, are summed up as:

- An accurate interpolation technique converges to the real function.
- An accurate interpolation technique handles special grids, e.g. boundary layer resolution.
- An accurate derivative of the interpolated flow variable, like pressure p, velocity $\mathbf{u}$, density ρ, temperature T, and entropy s, converges to the real derivative.
- A flexible algorithm assembles different hybrid aeroacoustic source terms, e.g. divergence of Lamb vector $\nabla\cdot(((\nabla\times\mathbf{u})\times\mathbf{u})')$ or entropy source $\nabla\cdot(T'\nabla\overline{s})$ [1].
- A conservative algorithm transfers the desired amount of energy, defined by the aeroacoustic sources, from the flow discretization to the mesh of the acoustic simulation.

Base on radial basis functions interpolation, we tackle the five challenges and propose a general method for the computation of the source terms. Compared to different interpolation algorithms, radial basis functions have promising capabilities: (1) the local behavior and the computational efficiency, known from nearest neighbor algorithms, is possible; (2) elegant computation of derivatives of the interpolated field; (3) patch search techniques indicate the resolution of typical flow structures. Radial basis functions allow us to use the primary flow variables velocity, pressure and density as input variables to compute aeroacoustic sources. We verify our approach by the "co-rotating vortex pair", with the divergence of Lamb vector as aeroacoustic source.

Radial Basis Function Interpolation

The main purpose of radial basis function interpolation is to interpolate flow results, such as velocity $\mathbf{u}$ or vorticity $\boldsymbol{\omega}$, from a computational fluid dynamics (CFD) grid to a computational aeroacoustics (CAA) mesh. Hybrid aeroacoustics deals with large problems and unfortunate data-distribution, e.g. boundary layers. Targeting these two challenges, we focus on a parallelizable algorithm that allows dynamic and local scaling of the basis function to handle distorted and ill-aligned datasets.

Global radial basis functions suffer from numerical instability of the different kernels and result in an unsatisfying interpolation quality. However, a local approach provides an accurate, and efficient interpolation. Following the local approach of Lazzaro[2], we first introduce two different source data patches (source point $\mathbf{x}$) around the target point $\mathbf{z}$, at which the interpolant is evaluated. Figure 1 defines the geometry. The set $X_q = \{\mathbf{x}_i \in \omega_s, i \in I_q\}$,

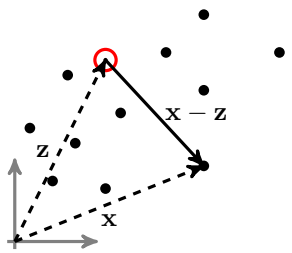

Figure 1: Geometric definitions of scattered data $(\mathbf{x}, \bullet)$ and the target point $(\mathbf{z}, \odot)$.

with I_q as the indices of the N_q neighbors of target-point, consists of N_q points, which define the patch-set. The second set $X_w = \{\mathbf{x}_i \in \Omega_s, i \in I_w\}$ with I_w as the indices of the N_w influence points, defines the influence for the different patches. The influence radius $r_{W_k} = \max_{k\in I_w}\{r_k\}$, with $r_k = ||\mathbf{x}_k - \mathbf{z}||_2$, is defined to be the maximum distance of a target point in X_w and $N_w \subset N_q$. The interpolant is given by

$$s(\mathbf{z}) = \sum_{k=1}^{N_q} \overline{W}_k(\mathbf{z}) R_k(\mathbf{z}), \tag{1}$$

where $R_k(\mathbf{z})$ defines the local interpolation system. The local interpolation system is given by the algebraic system

$$R_k(\mathbf{x}_k) = \sum_{j=1}^{N_q} c_j \Phi(||\mathbf{x}_j - \mathbf{x}_k||_2)\,, \tag{2}$$

which has to be solved initially for the N_q temporary (unscaled) interpolation-weights c_j, where $R_k(\mathbf{x}_k)$ denotes the scattered data (field that is interpolated) at patch-source-point $\mathbf{x}_k$. The weight function $\overline{W}_k$ of the modified interpolant $s(\mathbf{x})$ is chosen to be

$$\overline{W}_k(\mathbf{x}) = \frac{\left[\max\{\frac{(r_{W_k} - r_k)}{r_{W_k} r_k}, 0\}\right]^q}{\sum_{l=1}^{N_q} \left[\max\{\frac{(r_{W_k} - r_l)}{r_{W_k} r_l}, 0\}\right]^q}, \qquad (3)$$

with the exponent q as a measure of locality. The bigger q is, the more local the approach, therefore less accurate, but it can resolve stronger gradients. Then the interpolant $s(\mathbf{x})$ can be evaluated at every target point $\mathbf{z}$.

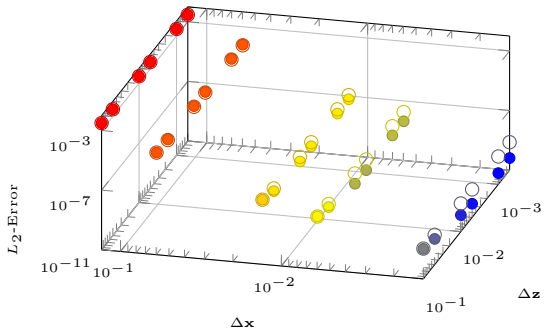

Figure 2: Convergence plot of the radial basis function interpolation with respect to the source discretization distance $\Delta\mathbf{x}$ and target discretization distance $\Delta\mathbf{z}$ of a regular mesh. The two search methods, "patch search" (bold), and nearest neighbor search (o), are compared.

Figure 2 shows the convergence of the radial basis function interpolation with respect to the source discretization distance $\Delta\mathbf{x}$ and target discretization distance $\Delta\mathbf{z}$ of a regular mesh. Obviously, there is an influence resulting from the source data density. In contrast, the target data density is not influencing the interpolation result. The graph reveals that both investigated search methods perform well.

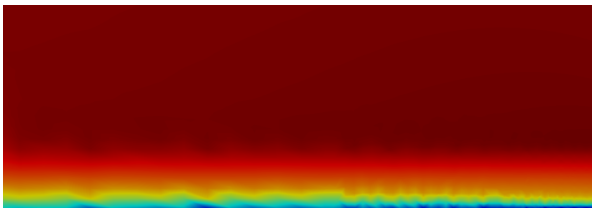

Figure 3: The velocity field of a CFD simulation was interpolated to a different grid with the ordinary nearest neighbor search algorithm. Non-physical artifacts occur in the boundary layer.

However, interpolations on boundary layer data shows that the nearest neighbor search method is failing for this odd data distributions. A standard nearest neighbor search produces a wavy pattern in the boundary layer (see Fig. 3). The boundary layer mesh is characterized by cells with a big edge ratio, e.g. 20-200. The phenomenon was analyzed considering interpolation data on slender cells with a ratio from 1-200. The results show that the nearest neighbor search based interpolation causes increasing errors for edge ratios over 20. Hence, the interpolation error for large edge ratios limits the application of the nearest neighbor search. If the source

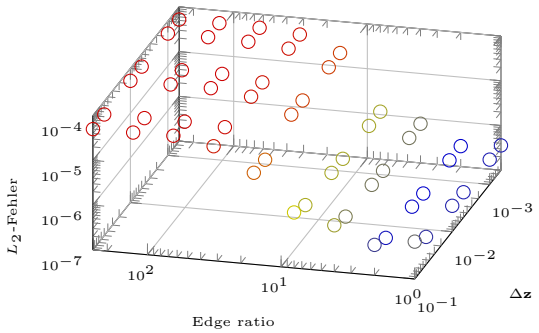

Figure 4: Convergence plot of the radial basis function interpolation with respect to the edge ratio of the source data. Nearest neighbor search was used.

data is computed via CFD, the data is based on an underlying grid. The conceptional different search strategy, "patch search", is based on the grid and the inherent connectivity of the cells. One cell is connected to neighbor cells, the first layer. Again, the first layer is surrounded by the second layer and so on. Figure 5 illustrates the search strategy for a target point in red and one layer of source data points. This hierarchical search strategy groups computational natural entities that are optimal source points for the interpolation. The boundary layer

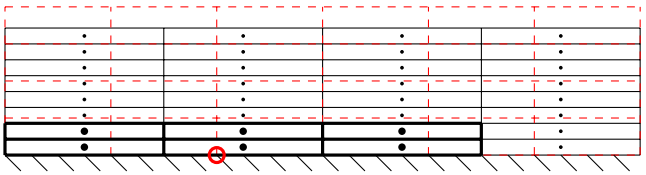

Figure 5: The patch search is based on the connectivity of the mesh. Starting from the red target point a containing source element is selected. From this source element, direct neighbors are selected by a layer strategy. This ensures that the natural neighborhood data transforms the data.

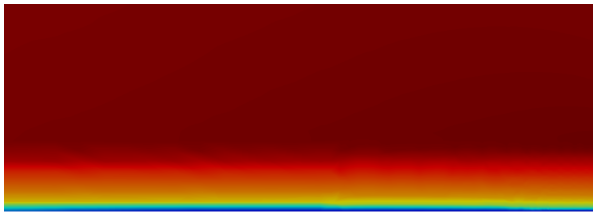

Figure 6: The velocity field of a CFD simulation was interpolated to a different grid with the "patch search" algorithm.

interpolation (Fig. 6) and the convergence plot (Fig. 7) show that the patch search strategy performs well for all investigated edge ratios, 1-200.

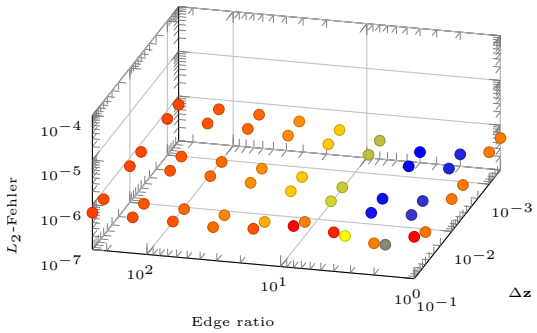

Figure 7: Convergence plot of the radial basis function interpolation with respect to the edge ratio of the source data. "Patch search" was used.

Radial Basis Function Derivatives

The main goal for this method is to construct a fast, scalable and accurate method to compute spatial derivatives, for the computation of aeroacoustic source terms. We define the local derivative method, similar as the interpolation, with the main difference in the definition of patches. For derivatives, there is only one source patch set $X_q = \{\mathbf{x}_i \in \Omega_s, i \in I_q\}$, with I_q as the indices of the N_q neighbours of target-point $\mathbf{z}$.

To compute the radial basis function derivative[3] of a given function $s(\mathbf{z})$ at target point $\mathbf{z}$, we apply the correct spatial derivative-operator $\mathcal{L}$ to the radial basis function and evaluate it, as presented in (4), where $\mathbf{x}_k$ and $\mathbf{x}_l$ are the coordinates of two source points with indices $k, l \in I_q$.

$$\mathcal{L}[\Phi_l(||\mathbf{z}-\mathbf{x}_k||_2)] = \sum_{l=1}^{N_q} c_l \Phi_l(||\mathbf{x}_l-\mathbf{x}_k||_2)\,, \quad k = 1, \cdots, N_q\,. \tag{4}$$

This system must be inverted, in order to obtain the weights c_l for the derivatives at the source points $l \in I_q$. Then the interpolant, derivative of $s(\mathbf{z})$, can be evaluated by

$$\mathcal{L}[s(\mathbf{z})] = \sum_{k=1}^{N_q} c_k s(\mathbf{x}_k) = \sum_{k=1}^{N_q} c_k R_k\,, \tag{5}$$

where $R_k = s(\mathbf{x}_k) \in \mathbb{R}^{N_q \times 1}$ is the scattered data value of the given function at source point $\mathbf{x}_k$. Depending on the choice of the kernel function Φ in (4), different methods can be obtained. In the following, the Gaussian kernel is used. This method computes derivative operators known from vector analysis (div, grad, curl). These vector analysis operators in conjunction with other data processing algorithms provide a flexible aeroacoustic source term evaluation procedure.

The convergence of radial basis function derivatives compared to finite difference on a regular grid analyzes the accuracy. Both stencils use 4 points (see Fig. 8). This study investigates the performance of radial basis functions with respect to the grid spacing h. Figure 9 shows that the order of convergence is as expected h^2. However, the radial basis function derivatives error increases for very fine meshes. At this point, the condition of the

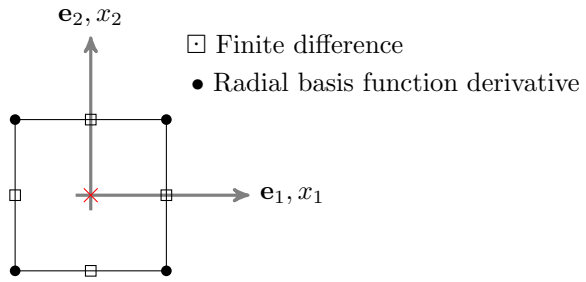

Figure 8: Stencil of derivatives displays the location of the source points of the derivatives under comparison.

system matrix rushes over the critical condition number and the during the inversion of the system matrix the local shape parameter is optimized towards a critical condition number.

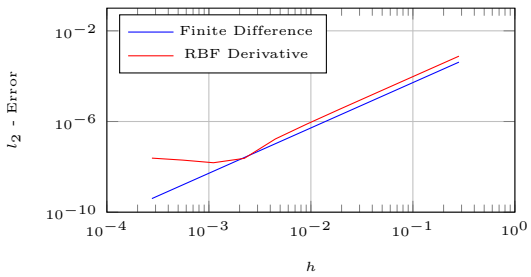

Figure 9: Convergence behavior of the radial basis function derivatives.

Application Example

The spinning vortex pair has been used frequently to determine the capabilities of aeroacoustic methodologies. The arrangement has the nature of a quadrupolar sound field.

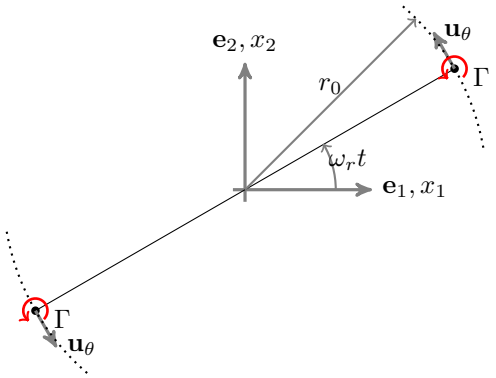

Figure 10: Schematic of the corotating vortex pair defining the main geometrical and physical characteristics.

Figure 10 illustrates the configuration of the vortex pair. Both vortices are delta distributions, and oppose each other at a distance of $2r_0$. Gaussians approximate the distributions. A circulation intensity Γ characterizes the strength of each vortex. The vortices rotate around the origin with a period of $T = 8\pi^2 r_0^2/\Gamma$, imposing an angular rotating speed $\omega_r = \Gamma/(4\pi r_0^2) \cdot \mathbf{e}_3 = \omega_r \cdot \mathbf{e}_3$. Each vortex convects the other vortex by a velocity of

$\mathbf{u}_\theta = \Gamma/(4\pi r_0) \cdot \mathbf{e}_t$, where $\mathbf{e}_t$ is the unit vector in tangential direction. The Mach number in the circumferential direction is given by $M_\theta = u_\theta/c = \Gamma/(4\pi r_0 c)$. Müller and Obermeier [4] derived an analytic solution of the acoustic far-field, based on matched asymptotic expansion of the potential solution.

The analytical solution judges our simulations using the vortex sound equation [5]

$$\frac{1}{c^2}\frac{\partial^2}{\partial t^2}p' - \nabla \cdot \nabla p' = \bar{\rho}\nabla \cdot (\boldsymbol{\omega} \times \mathbf{u}) \,. \tag{6}$$

In (6) p' denotes the fluctuating pressure, c the isentropic speed of sound, $\bar{\rho}$ the mean density, $\mathbf{u}$ the velocity and $\boldsymbol{\omega}$ the vorticity. The computation of the source term involves the curl of the velocity, the assembling of the Lamb vector and the computation of its divergence. Finally, a conservative integration projects the energy of the source term onto the acoustic grid. Since using radial basis function derivatives, this workflow has been the most promising with respect to the acoustic simulation results. Figure 11 shows the coarse discretization, about 5 elements over a vortex, and the fine discretization, 3 times finer then the coarse mesh. Based on this two

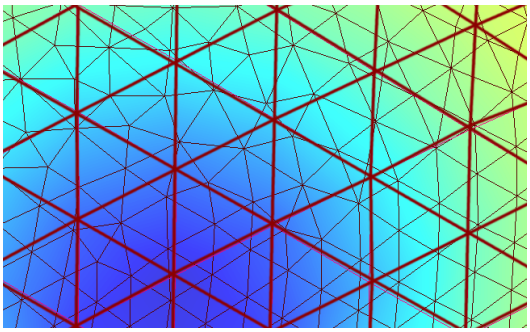

Figure 11: Coarse and fine mesh discretizing one vortex.

meshes we computed the acoustic field (see Fig. 12). The rotating quadrupole expresses the expected field pattern. A comparison between the analytic solution and the two discretizations show that both meshes are able to compute accurate sources and respectively the acoustic field (see Fig. 13).

Figure 12: Acoustic field of the vortex pair.

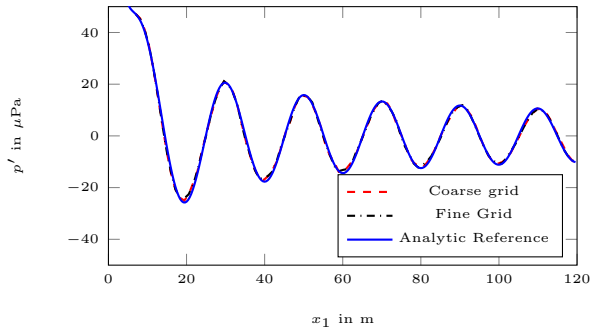

Figure 13: Comparison of the acoustic pressure p' as a function of the coordinate x for different discretizations.

Conclusion

We investigate the coupling step, also named interpolation, of the hybrid aeroacoustic approach. The desired properties of the coupling scheme are analyzed using radial basis function interpolation. We revealed promising capabilities of radial basis function for the following five challenges being necessary in hybrid aeroacoustic approaches. First, radial basis function interpolation converges to the real function. Second, radial basis function interpolation in conjunction with the "patch search" strategy handles special grids, e.g. boundary layer resolution. Third, the derivatives converge to the real derivative with the same order as finite differences. Fourth, a flexible framework was developed to assemble different hybrid aeroacoustic source terms. The computation and assembly of the source terms happens on the CFD grid, since this is the natural discretization, resolving all possible scales in fluid dynamics. Fifth, a conservative interpolation from the CFD grid to the acoustic mesh ensures energy conservation. The verification of our approach by the co-rotating vortex pair solidifies our method.

References

[1] R. Ewert, and W. Schröder: On the simulation of trailing edge noise with a hybrid LES/APE method. Journal of Sound and Vibration 270.3 (2004), 509-524.

[2] D. Lazzaro, and L. Montefusco: Radial basis functions for the multivariate interpolation of large scattered data sets. Journal of Computational and Applied Mathematics 140 (2002), 521536

[3] Larsson, Elisabeth, et al.: Stable computation of differentiation matrices and scattered node stencils based on Gaussian radial basis functions. SIAM Journal on Scientific Computing 35.4 (2013), A2096-A2119.

[4] Müller, E. A., and F. Obermeier: The spinning vortices as a source of sound. AGARD CP-22 (1967), 22-1.

[5] Howe, Michael S.: Theory of vortex sound. Vol. 33. Cambridge University Press, 2003.